

Evidence for an Aspherical Population III Supernova Explosion Inferred from the Hyper-metal-poor Star HE 1327–2326*

Abstract

We present observational evidence that an aspherical supernova explosion could have occurred in the first stars in the early universe. Our results are based on the first determination of a Zn abundance in a *Hubble Space Telescope*/Cosmic Origins Spectrograph high-resolution UV spectrum of a hyper-metal-poor (HMP) star, HE 1327–2326, with [Fe/H](NLTE) = -5.2. We determine [Zn/Fe] = 0.80 ± 0.25 from a UV Zn I line at 2138 Å, detected at 3.4σ . Yields of a $25\,M_\odot$ aspherical supernova model with artificially modified densities exploding with $E=5\times10^{51}$ erg best match the entire abundance pattern of HE 1327–2326. Such high-entropy hypernova explosions are expected to produce bipolar outflows, which could facilitate the external enrichment of small neighboring galaxies. This has already been predicted by theoretical studies of the earliest star-forming minihalos. Such a scenario would have significant implications for the chemical enrichment across the early universe, as HMP carbon-enhanced metal-poor (CEMP) stars such as HE 1327–2326 might have formed in such externally enriched environments.

Key words: Galaxy: halo – stars: abundances – stars: individual (HE 1327-2326) – stars: Population II – stars: Population III – supernovae: general

1. Introduction

Our knowledge of the nature, formation, and properties of the Population III (Pop III) stars and their first supernova explosions (SNe) has been driven mainly by theoretical work and cosmological simulations (Bromm et al. 2009; Greif et al. 2010). These studies have, for example, predicted a large range of masses for the first stars over the past decade, from $<1\,M_\odot$ to $>1000\,M_\odot$ (Omukai & Palla 2001; Yoshida et al. 2006; Stacy et al. 2012; Hartwig et al. 2015). More generally, evidence on the first stars and SNe can be obtained from the chemical signatures of surviving low-mass, ultra-metal-poor (UMP) stars with $[{\rm Fe/H}]^{12} < -4.0$ (Beers & Christlieb 2005). They likely formed from gas enriched by individual first-SNe events whose chemical signatures they have retained over billions of years (Frebel & Norris 2015; Hartwig et al. 2018).

Theoretical SNe nucleosynthesis yielding calculations of Pop III progenitors have long been invoked to explain the origins of the observed abundance patterns in UMP stars (Woosley & Weaver 1995; Umeda & Nomoto 2002; Iwamoto et al. 2005; Tominaga et al. 2007b; Heger & Woosley 2010;

Grimmett et al. 2018). Early spherical SNe models were not able to attain both the α -element and iron-peak (Mn, Co, Zn) abundance enhancements relative to iron (Cayrel et al. 2004), irrespective of the explosion energies employed (Woosley & Weaver 1995). Neither could they simultaneously produce the observed very large light element [C, N, O/Fe] > 1 ratios found in most UMP stars.

To better reproduce these ratios, a "mixing and fallback" (MF) model was developed (Umeda & Nomoto 2002), defined by three parameters to account for aspherical effects, namely (i) the initial mass cut that corresponds to the inner boundary of the mixing region (M_{cut}) , (ii) the outer boundary of the mixing region (M_{mix}) , and (iii) the ejection factor (f) corresponding to the fraction of matter ejected from the mixed region. Two different mechanisms can be mimicked by the MF process (as shown in Figures 12(a) and (b) in Tominaga et al. 2007b). The first mechanism is faint, quasi-spherical MF SNe (with explosion energies $E \leq 10^{51}$ erg) that experience significant gravitational fallback of material onto the nascent black hole. Before the fallback, Rayleigh-Taylor instabilities induce mixing (Joggerst et al. 2010) of the products of complete silicon burning (e.g., calcium, titanium, and iron) with material from the carbon-oxygen core. The second mechanism is aspherical bipolar jet SNe that experience significant gravitational fallback of material onto the nascent black hole along the equatorial plane and ejection of material from the complete Siburning layers along the jets (Tominaga et al. 2007a;

^{*} Based on observations made with the NASA/ESA *Hubble Space Telescope*, obtained at the Space Telescope Science Institute (STScI), which is operated by the Association of Universities for Research in Astronomy, Inc. (AURA) under NASA contract NAS 5-26555. These observations are associated with program GO-14151.

¹² Defined as [A/B] = $\log_{10}(N_A/N_B)_{\text{star}} - \log_{10}(N_A/N_B)_{\odot}$, with N_A and N_B being the respective element number densities.

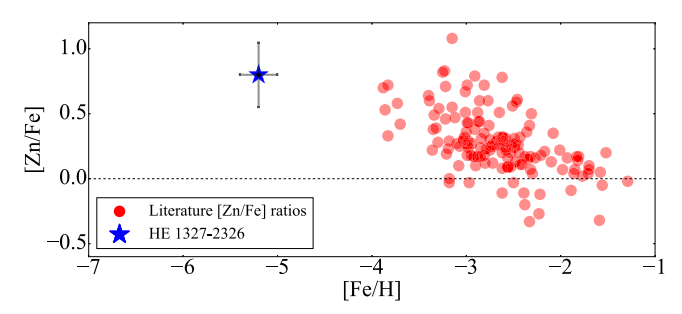


Figure 1. [Zn/Fe] abundance ratios for metal-poor stars with -4 < [Fe/H] < -1 from Cayrel et al. (2004), Barklem et al. (2005), Hollek et al. (2011), and Jacobson et al. (2015). The [Zn/Fe] = 0.80 ± 0.25 obtained in this work for HE 1327–2326 at $[Fe/H] = -5.20 \pm 0.20$ is shown by the blue star and black error bars. Abundance values are extracted from the JINAbase (Abohalima & Frebel 2018).

Tominaga 2009). Both mechanisms result in the ejection of a relatively small (residual) amount of iron but a comparably large amount of, e.g., carbon (Umeda & Nomoto 2002). This way, the large ratios of [C/Fe], [N/Fe], and [O/Fe] in UMP stars are produced.

The difference between the two mechanisms, however, appears in the abundance ratios among Fe-peak elements. In the former quasi-spherical faint explosion model, large Zn and other iron-peak elemental abundances cannot be obtained (Tominaga 2009; Nomoto et al. 2013; Grimmett et al. 2018) because a weak explosion energy is required to achieve the extensive fallback (necessary for producing a low iron abundance). On the other hand, in the aspherical bipolar jet explosion model, the high-entropy environment along the jets enables large [Zn/Fe] ratios because more Zn is ejected. Studies of extremely metal-poor (EMP) stars with -4.5 < [Fe/H] < -3 have indeed shown enhanced [Zn/Fe] > 0 ratios (Figure 1; abundance data from Cayrel et al. 2004; Barklem et al. 2005; Hollek et al. 2011; Jacobson et al. 2015; abundances extracted from the JINAbase¹³; Abohalima & Frebel 2018), thus favoring the aspherical explosion model.

But no zinc measurements have thus far been possible for stars with [Fe/H] < -4.5 due to the intrinsic weakness of the strongest optical zinc triplet lines at 4680 Å, 4722 Å, and 4810 Å. However, another strong Zn I line exists in the UV spectral range at 2138 Å. Unfortunately, all stars with [Fe/ H] < -4.5 are much too faint for successful UV observations —with the exception of HE 1327–2326, a Milky Way halo HMP star with [Fe/H](NLTE) = -5.2 (Ezzeddine & Frebel 2018). This star has been extensively studied based on optical spectra (Frebel et al. 2005, 2008; Aoki et al. 2006; Korn et al. 2009). To continue to provide the most stringent observational constraints on the explosion mechanism, the details of the progenitor star and the origin of Zn in UMP stars, we obtained a Hubble Space Telescope/Cosmic Origins Spectrograph (HST/COS) high-resolution UV spectrum for HE 1327-2326 in which we detected the absorption line of zinc at 2138 Å for the first time.

We describe the UV observations and data reduction in Section 2 and the chemical abundance analysis in Section 3. We use the $[\mathrm{Zn/Fe}]$ ratio in HE 1327–2326 to constrain the SNe properties of its first star progenitor in Section 4, and present our interpretations and conclusions in Section 5.

2. Observations and Data Reduction

We obtained UV observations of HE 1327-2326 with the COS on board the HST (Program ID: GO-14151), from 2016 May to July 15. The spectrum covers the three wavelength regions: 2118-2151 Å, 2216-2249 Å, and 2315-2348 Å. The total integration time was 22 hr and 20 minutes. We performed a custom data reduction to optimize the signal-to-noise (S/N)ratio of the final spectrum. By default, the COS extraction pipeline, CALCOS (Fox et al. 2015), uses an extraction box height of 56 pixels in the cross-dispersion ("y") direction to extract the three stripes from the exposures. This procedure ensures that virtually all the source flux is captured, but at the cost of summing over pixels where the raw S/N is very low. Alternatively, we used an extraction box height of nine pixels in the cross-dispersion direction. This height collects somewhat less than the total source flux (at the 10% level) and so can be used safely for line-to-continuum contrast measurements but not for cases where precise spectro-photometric measurements are necessary for the science. In our case, the vertical (crossdispersion or "y") location of the 9 pixel extraction boxes was tuned individually for each stripe in each exposure using the B_SPEC and HEIGHT parameters in the XTRACTAB reference file, and the edge-to-edge slope (SLOPE) in the diagonal boxes was retained at their default values. This is the procedure recommended by the STScI COS instrument team (Snyder & Sonnentrucker 2017). More details on the extraction, co-addition, and normalization of the final UV spectrum can also be found in Ezzeddine & Frebel (2018).

One Zn I line at 2138.57 Å, five Fe II lines, and one Si I line, were detected in the final UV spectrum. Figure 2 shows parts of these detections. For visual purposes, the bottom right panel (f) of Figure 2 shows the Zn I line region smoothed with an average boxcar of 2 pixel width. The abundances of Fe and Si were determined and discussed further in Ezzeddine & Frebel (2018).

3. Chemical Abundance Analysis

3.1. Fundamental Stellar Parameters

In our abundance analysis of HE 1327–2326, we use an effective temperature of $T_{\rm eff}=6180\pm80$ K, derived from color-effective temperature relations using broadband *UBVRI* photometry (Frebel et al. 2005), a surface gravity of $\log g=3.7\pm0.2$ and a microturbulent velocity of $\xi_t=1.7$ km s⁻¹ based on previous studies (Korn et al. 2009; Ezzeddine & Frebel 2018). The *Gaia* second data release DR2 (Gaia Collaboration et al. 2018) produced $T_{\rm eff}=5915\pm300$ K and $\log g=3.40\pm0.3$ based on photometric colors and parallax, respectively. We use both sets of stellar parameters to determine the [Zn/Fe] abundance ratio of HE 1327–2326. We employ a standard model atmosphere (Castelli & Kurucz 2004) with an input model metallicity of [Fe/H] = -5.0 and α -enhancement [α /Fe] = 0.4 throughout.

3.2. [Zn/H] and [Zn/Fe] Abundances in HE 1327-2326

We measure an equivalent width of $43.4 \pm 12.7 \,\text{mÅ}$ for the Zn I line at $2138.57 \,\text{Å}$, by convolving the COS line-spread functions (Ghavamian et al. 2009) with Gaussian profiles following Roederer et al. (2016). We determine uncertainties in the equivalent width and Zn abundance measurements by altering the continuum placement and the FWHM of the

¹³ https://jinabase.pythonanywhere.com

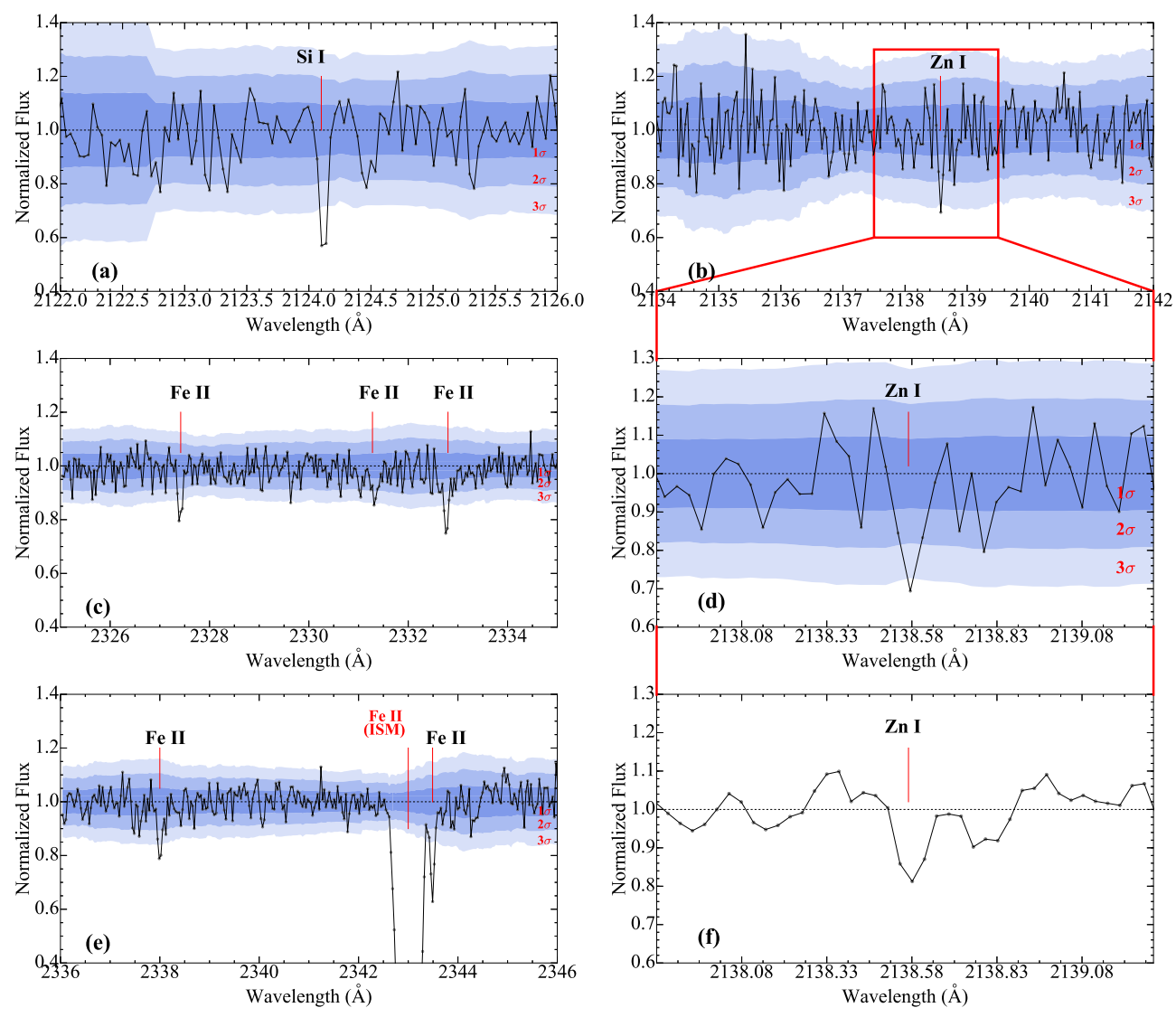


Figure 2. Selected regions of the co-added UV spectrum of HE 1327–2326, where atomic lines of Si I, Zn I, and Fe II were detected for the first time. The Fe II interstellar medium (ISM) line at 2343 Å is also detected, as shown in panel (e). The detection significance levels of the lines are shown by the different shaded areas: 1σ (darkest blue), 2σ (light blue), and 3σ (lightest blue). For clarification purposes, panel (f) shows a smoothed part of the spectrum centered around the Zn line at 2138.57 Å, and covering the same spectral range as panel (d). The spectrum was smoothed using an average boxcar smoothing with a 2.0 pixel width. For completeness, we also show the Si I and Fe II spectral line regions, studied in detail in Ezzeddine & Frebel (2018).

spectral line by $\pm 1\sigma$, and recording the corresponding changes. We assess a detection significance of 3.4σ by dividing the equivalent width of the line by its uncertainty. We then calculate the abundance of Zn using the equivalent width curve-of-growth method using the local thermodynamic equilibrium (LTE) radiative transfer code MOOG updated to include proper scattering treatment (Sneden 1973; Sobeck et al. 2011), and with custom analysis tools (Casey 2014). The abundances are determined relative to the solar values from Asplund et al. (2009).

Using $T_{\rm eff}=6180$ K and $\log g=3.7$ (Frebel et al. 2008), we determine a Zn abundance of $[{\rm Zn/H}]=-4.40\pm0.25$ using the 1D, LTE framework. The conditions of line formation in metal-poor stars are known to deviate from the assumptions of LTE and 1D model atmospheres (Thévenin & Idiart 1999; Takeda et al. 2005; Mashonkina et al. 2011; Bergemann et al. 2012). Abundances from lines of minority species, such as neutral Zn I and Fe I, are often prone to larger non-local thermodynamic equilibrium (NLTE) effects in the atmospheres

of low-metallicity stars than from lines of the corresponding dominant ionized species. Investigations of possible NLTE effects for abundances of commonly used optical Zn I lines over a range of stellar parameters showed that NLTE abundance corrections, defined by the differences between the NLTE and LTE abundances using the same observed equivalent widths, are actually not significant and ≤0.2 dex (Takeda et al. 2005). Even though the departures from LTE have not been calculated explicitly for any UV Zn I lines, it could be shown by Roederer & Barklem (2018) that ionization equilibrium in LTE can be reached in metal-poor stars with -3.0 < [Fe/H] < -1.0 (within 0.1 dex) using optical (e.g., Zn I λ 4810) and UV (e.g., Zn II λ 2062) lines. Departures from LTE for Zn were indeed insignificant, even at [Fe/H] = -3.0. Following these results, we assume that our LTE Zn abundance, as derived from the UV line, would be compatible with values obtained from any optical lines, if ever detected.

For Fe, however, strong NLTE effects have been well documented (e.g., Asplund 2005, and references therein). We

Table 1
Chemical Abundances of 13 Elements Determined from the UV and Optical Spectra of HE 1327-2326

El	N _{nlines}	$\log \epsilon(X)$	$\sigma \log \epsilon(X)$	[X/H]	[X/Fe]
C (CH)	syn.	6.21ª	0.10	-2.22	3.49
N (NH)	syn.	6.10 ^a	0.20	-1.73	3.98
O (OH)	syn.	6.12 ^a	0.20	-2.57	3.14
Na I	2	2.99	0.04	-3.25	2.46
Mg I	4	3.54	0.02	-4.06	1.65
Al I	1	1.90	0.03	-4.55	1.16
Si I ^b	1	2.80	0.27	-4.71	1.28
Ca II	4	1.34	0.15	-5.00	0.71
Ti II	15	-0.09	0.17	-5.04	0.67
Fe I ^c	10	1.79	0.15	-5.71	
Fe I ^d	10	2.30	0.11	-5.20	•••
Fe II	4	1.51	0.26	-5.99	
Ni I	4	0.73	0.20	-5.49	0.33
Zn I	1	+0.16	0.25	-4.40	0.80
Sr II	2	-1.76	0.06	-4.63	1.08
Sc II	•••	<-1.68		<-4.83	< 0.88
Mn I	•••	< 0.53		<-4.90	< 0.81
Co I	•••	< 0.58		<-4.41	<1.30

Notes. Upper limits for Sc, Mn, and Co are also included.

thus adopt the 1D, NLTE Fe abundance of [Fe/H] = -5.20 in HE 1327–2326, inferred from 10 Fe I optical lines as determined in Ezzeddine & Frebel (2018). This Fe abundance for HE 1327–2326 is based on detailed investigations of possible 3D and NLTE effects on both Fe I and Fe II lines in the optical and UV. We then obtained a zinc to iron abundance ratio of $[Zn/Fe] = 0.80 \pm 0.25$. For completeness, we note that any potential NLTE correction to the Zn I abundance (should they exist) would be positive, and would thus only further increase the [Zn/Fe] ratio (Takeda et al. 2005).

We also investigate the [Zn/Fe] abundance ratio using *Gaia* DR2 stellar parameters, which yield slightly lower 1D, LTE Zn and 1D, NLTE Fe abundances of [Zn/H] = -4.70 and [Fe/H] = -5.40, respectively. This 1D, NLTE abundance of Fe was determined following the same setup used in Ezzeddine et al. (2017). Compared to our other value, the [Zn/Fe] decreases only slightly, to 0.70 ± 0.25 . This shows that the [Zn/Fe] ratio in HE 1327–2326 is robustly enhanced, irrespective of the choice of stellar parameters.

To establish the overall [X/Fe] abundance pattern of HE 1327–2326, we adopt [Zn/Fe] = 0.80 ± 0.25 , in addition to the UV Si I abundance from Ezzeddine & Frebel (2018), as well as the optical abundances for 11 elements and upper limits for 5 others (Sc, V, Cr, Mn and Co) from Frebel et al. (2008). All elemental abundances used are listed in Table 1. We use this pattern to compare to the theoretical SNe nucleosynthesis yields of various models.

4. Constraining the Pop III Star Explosion Properties

4.1. Comparison to Faint MF Quasi-spherical SNe Models

Previous studies have commonly compared abundance patterns of individual UMP stars, such as that of HE 1327 –2326, to the yields of faint MF quasi-spherical Pop III SNe

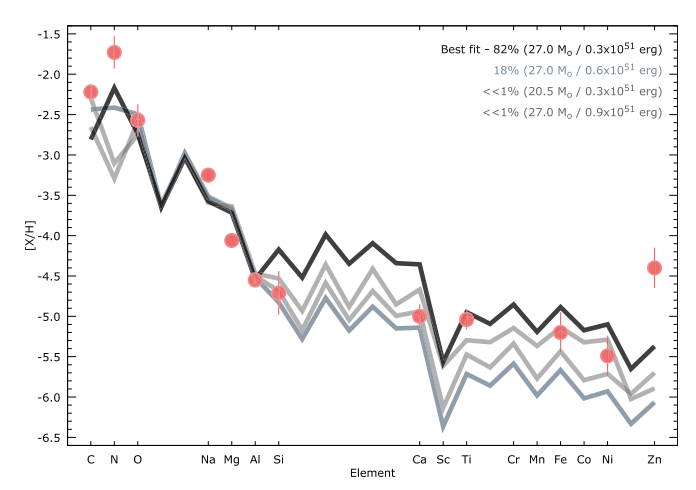


Figure 3. Statistical results for comparisons of a large grid of (16,800) MF (quasi-spherical) SNe nucleosynthesis yields (Heger & Woosley 2010) with different progenitor masses and explosion energies, to 10,000 re-sampled chemical abundance patterns of HE 1327–2326.

(Umeda & Nomoto 2002; Christlieb et al. 2004; Frebel et al. 2005; Iwamoto et al. 2005; Keller et al. 2014; Bessell et al. 2015; Placco et al. 2016; Nordlander et al. 2017). As discussed in Section 1, such spherical explosions underproduce iron-peak elements (such as Co, Cr, or Zn) (Tominaga 2009; Grimmett et al. 2018; Hirai et al. 2018; Tsujimoto & Nishimura 2018). Due to a lack of iron-peak abundances, the comparisons of the data with these model results usually remained unconstrained in the that region. With available Zn abundances, however, new constraints can be obtained.

We perform statistical fitting tests following Placco et al. (2016), to compare the determined abundance pattern of HE 1327–2326 (including Zn) to 16,800 theoretical yields ¹⁴ of quasi-spherical MF SNe models, computed with different explosion parameters (e.g., progenitor mass, explosion energies, mixing parameters). To account for uncertainties in our fitting results, we simulate 10,000 different abundances for each observed element used in the fit, which follow a normal distribution centered around the measured abundance (taken as the mean). We then randomly sample the abundance distributions for all elements and generate 10,000 artificial abundance patterns for HE 1327–2326, to compare the yields. Our results, shown in Figure 3, demonstrate that indeed none of the mixingfallback supernova models can match the Zn abundance (relative to Fe) in HE 1327-2326. Overall, 82% of the simulated abundance patterns of HE 1327-2326 can be fit best (although not satisfactorily) with a $27 M_{\odot}$ progenitor exploding with 0.3×10^{51} erg. Of the simulated abundance patterns, 18% are also reproduced by a 27 M_{\odot} progenitor, but with a slightly higher explosion energy of 0.6×10^{51} erg. The remaining few abundance patterns («1%) are fit best with $20.5\,M_{\odot}$ and $27\,M_{\odot}$ progenitors with $0.3\times10^{51}\,\mathrm{erg}$ and 0.9×10^{51} erg, respectively.

Building on these results, we can statistically rule out faint quasi-spherical SNe as the source of metals in HE 1327–2326, as no superposition of yields would produce enough Zn relative to the lighter elements. Enrichment by multiple events can also more broadly be eliminated following the theoretical monoenrichment classification scheme suggested by Hartwig et al. (2018), in which stars with -6.0 < [Fe/H] < -4.0 and [Mg/H]

^a 3D values adopted from Frebel et al. (2008).

^b Adopted from Ezzeddine & Frebel (2018).

^c LTE abundance from Frebel et al. (2008).

^d NLTE abundance adopted from Ezzeddine & Frebel (2018).

¹⁴ Models from https://2sn.org/starfit/ (Heger & Woosley 2010).

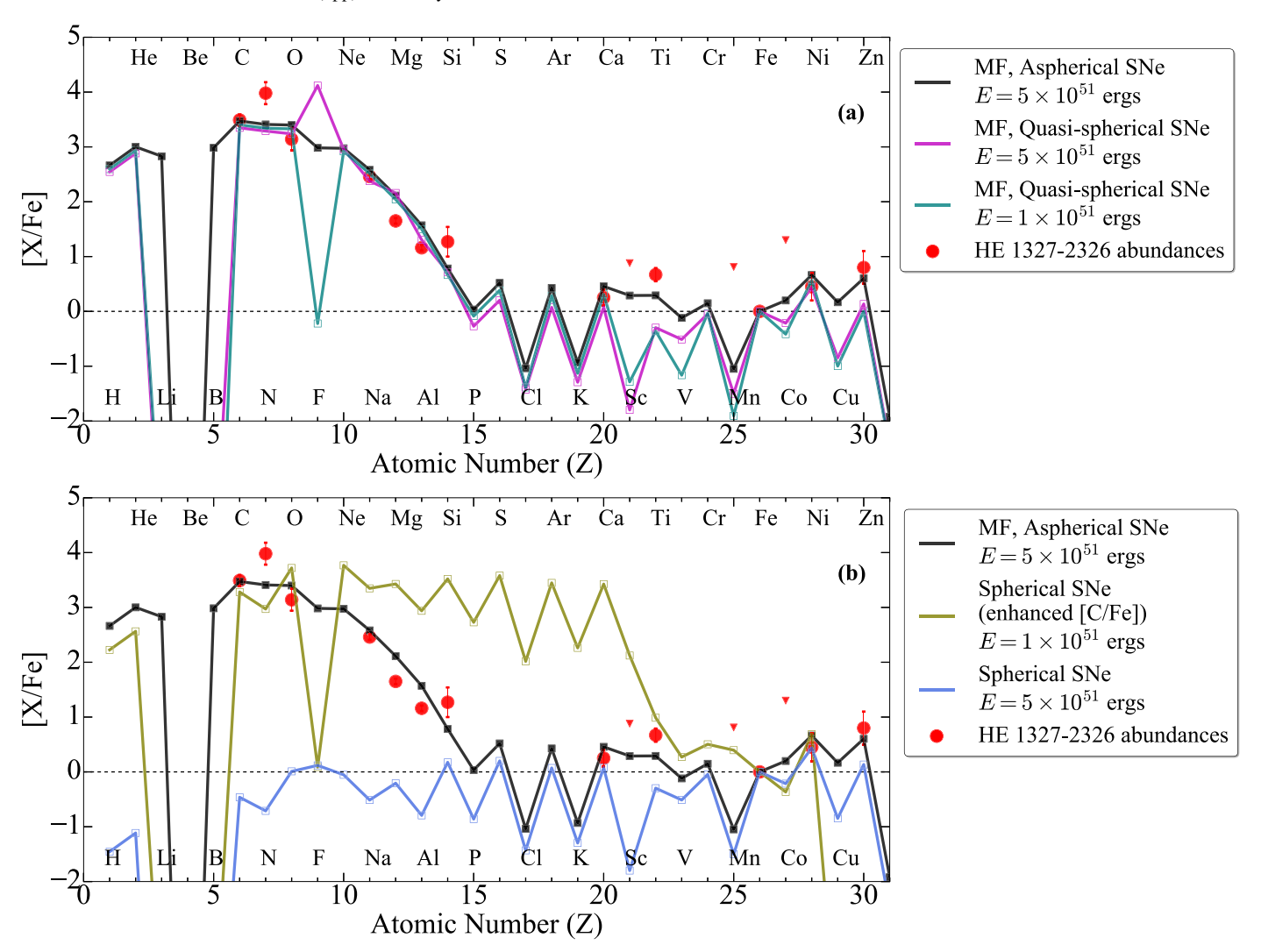


Figure 4. Best-fit predicted yields of a density-modified "mixing and fallback" mimicking an aspherical SNe explosion model with bipolar outflows of a first star progenitor with $25 M_{\odot}$ and $E_{51} = 5 \times 10^{51}$ erg explosion energy (black solid line). This is obtained from fitting various models and associated parameters to the measured abundance pattern of HE 1327−2326 (red symbols). Triangles indicate upper limits. Panel (a) also shows yields for two $25 M_{\odot}$ quasi-spherical MF explosion models with explosion energies of $E = 1 \times 10^{51}$ erg (solid teal line) and $E = 5 \times 10^{51}$ erg (solid magenta line), respectively. Panel (b) shows yields for two spherical SNe explosion models with $E = 1 \times 10^{51}$ erg and an enhanced [C/Fe] ratio (solid gold line), and $E = 5 \times 10^{51}$ erg (solid blue line), respectively. Only the density-modified, aspherically mimicked model with bipolar jets is able to reproduce the largely enhanced [Zn/Fe] abundance ratio determined in HE 1327−2326.

C] < -1.0 have a strong likelihood of being enriched by a single SNe event. This applies well to HE 1327-2326 with [Fe/H] = -5.2 and [Mg/C] = -1.84. Overall, this shows that the progenitor of HE 1327-2326, and possibly those of other UMP stars with similar abundance patterns, did not explode (quasi-)spherically.

4.2. Comparison to Aspherical SNe Models

We compare the abundance pattern of HE 1327–2326 to the yields of density-modified MF models with different masses and explosion energies, thus mimicking aspherical SNe with bipolar outflows. Specific details on the explosion models and yield calculations are described in Tominaga et al. (2007b). We find that the yields of a 25 M_{\odot} first star progenitor exploding with an aspherical SNe, with a high explosion energy of $E=5\times10^{51}$ erg, best matches the entire abundance pattern of HE 1327–2326, including zinc. We show this result with the black solid line in Figure 4. Our best-fit model has an initial mass cut of $M_{\rm cut}=1.64\,M_{\odot}$, outer boundary mixing region mass of $M_{\rm mix}=5.65\,M_{\odot}$, and ejection factor of f=0.0002.

To specifically increase the zinc yield of an MF SNe model, the explosion mechanism was modified such that the matter density is artificially reduced, to mimic a high-entropy explosion environment, which is required for increased explosive nucleosynthesis (Maeda & Nomoto 2003; Tominaga et al. 2007a, 2007b; Grimmett et al. 2018). In this modified framework, elements formed in the deepest layers during the explosion, such as zinc, are (at least partially) mixed upward and then ejected. This occurs alongside the release of only small amounts of iron (most iron falls back onto the nascent black hole) and large amounts of, e.g., carbon made in the layers farther out. The density-modified MF model thus parameterizes what would physically be an aspherical SNe with bipolar outflows or jets (see panel (b) of Figure 12 in Tominaga et al. 2007b), with the ejection factor f in the 1D model being equivalent to the fraction of the solid angle of the region where the ejected mass elements in the Si-burning layer are located in the 2D model (i.e., f = 1 in the spherical model). The necessary high-entropy environment would occur along the rotation axis. Tominaga (2009) showed that the abundance

 Table 2

 Parameters of the Different SNe Model Yields Used in Figure 4

Model	Mass (M_{\odot})	E (10 ⁵¹ erg)	$M_{ m cut} \ (M_{\odot})$	$M_{ m mix} \ (M_{\odot})$	f
Mixing and Fallback, density-modified aspherical	25	5	1.64	5.65	0.0002
Mixing and Fallback, quasi-spherical, high energy	25	5	1.59	5.69	0.0001
Mixing and Fallback, quasi-spherical, low energy	25	1	1.61	5.65	0.00015
Spherical, enhanced [C/Fe]	25	1	2.24	•••	1
Spherical	25	5	1.59	•••	1

patterns of the yields of the 2D aspherical bipolar explosion are reproduced by the density-modified MF model. Unfortunately, more realistic 3D explosion models of metal-free stars are not available yet to further investigate this behavior.

We also explore other geometries using the same progenitor mass of $25 M_{\odot}$ including two quasi-spherical MF SNe models with low $(E = 1 \times 10^{51})$ erg; teal solid line in panel (a) of Figure 4) and high $(E = 5 \times 10^{51})$ erg; magenta solid line in panel (a) of Figure 4) explosion energies. Two spherical SNe models with and without enhanced [C/Fe] ratios were also explored, corresponding to, respectively, the gold and blue solid lines in panel (b) of Figure 4. The explosion parameters M_{cut} , M_{mix} , and f used for each of these models are listed in Table 2. Both quasi-spherical MF models with $E = 1 \times 10^{51}$ erg and $E = 5 \times 10^{51}$ erg are not able to produce the [Zn/Fe] > 0 ratio. Simultaneously, they also underreproduce the [Sc/Fe] and [Ti/Fe] ratios compared to the aspherical model. The explosive nucleosynthesis in the densitymodified, high-entropy aspherical model enhances the α -rich freezeout, thus enhancing the [Sc/Fe] and [Ti/Fe] ratios usually determined in EMP stars with [Fe/H] < -3 (Tominaga et al. 2007b). Given that the determined [Ti/Fe] = 0.67ratio in HE 1327-2326 is enhanced, an aspherical explosion model is thus clearly favored.

We note that spherical models could principally also produce a high-entropy environment, and hence a solar [Zn/Fe] ratio if the explosion energy were large enough, e.g., $E=5\times10^{51}$ erg (see panel (b) of Figure 4; Nomoto et al. 2013). However, such an energetic explosion would be highly inconsistent with the significant fallback required to produce the low Fe abundances observed in UMP stars, including HE 1327–2326. This explains why the spherical models are unlikely contenders for the explosion mechanisms of the HE 1327–2326 progenitor, and perhaps even for other first stars.

Overall, the explosion of the massive Pop III star progenitor of HE 1327–2326 is thus more energetic than previously thought (i.e., a hypernova), in line with more recent studies, such as Grimmett et al. 2018. Interestingly, previous work has suggested that only faint MF-first SNe would seed carbonenhanced metal-poor (CEMP) stars such as HE 1327–2326, because their host minihalos would be disrupted by any larger energy input (Cooke & Madau 2014). Our results provide an alternative explanation, as high-energy aspherical SNe explosions could also produce high [C/Fe] ratios.

4.3. Evidence for Aspherical Explosions from Rotation

It has been proposed that aspherical SNe are driven by (fast) rotating progenitors with possibly strong magnetic fields (Maeda & Nomoto 2003; Meynet et al. 2006; Ekström et al. 2008). This is in line with theoretical predictions that the first

stars were heavily rotating (Meynet et al. 2006; Stacy et al. 2011; Tsujimoto & Nishimura 2018). Indeed, the progenitors of HE 1327–2326 and those of other second-generation stars have already been shown to be fast-rotating based on their large relative nitrogen abundance ratios, e.g., [N/Fe] = 3.98 in HE 1327–2326, [N/Fe] = 2.57 in HE 0107–5240 (Christlieb et al. 2004), and [N/Fe] = 3.46 in SD 1313–0019 (Frebel et al. 2015).

Stellar surface nitrogen abundances become enhanced due to internal mixing caused by rotation (Meynet et al. 2006; Choplin et al. 2017), rather than being produced during their explosion (see Figure 4). Additionally, Maeder et al. (2015) and Choplin et al. (2018) have proposed that a fast-rotating Pop III star progenitor could be responsible for the enhanced [Sr/Fe] = 1.08 determined for HE 1327–2326 and other EMP stars with [Sr/Fe] > 0.5. They showed that fast rotation in a low-metallicity, massive star can set off a strong mixing between the H- and He-burning zones, which triggers the synthesis of Sr and other light neutron-capture elements made in the s-process.

Introducing rotation of Pop III stars into the standard neutrino-driven paradigm of core-collapse supernovae has independently been shown to lead to bipolar (jet-like) SNe (Fryer & Heger 2000; Burrows et al. 2004). Finally, rotation has also been implemented into early universe and first-stars cosmological simulations (Greif et al. 2010; Stacy et al. 2011) to investigate the ab initio formation of the first stars. Moreover, Tsujimoto & Nishimura (2018) recently predicted through their galactic chemical evolution calculations that magneto-rotational driven explosions could indeed be the dominant source of enhanced [Zn/Fe] abundance ratios in the Milkv Wav satellite dwarf galaxy stars with -4 < [Fe/H] < -1.

4.4. vp-process in SNe: Is it Able to Produce the Enhanced [Zn/Fe] in HE 1327–2326?

Fröhlich et al. (2006a) and Pruet et al. (2006) proposed that increasing the entropy by increasing the electron mole fractions Y_e in a faint quasi-spherical SNe model to values >0.5 would mimic a νp -process in the neutrino-driven winds emerging from the proto-neutron star of the Pop III progenitor. This could enhance the production of [Sr/Fe] as well as the iron-peak elements [Sc,Co,Zn/Fe] ratios, as is observed in UMP stars.

Fröhlich et al. (2006b), however, showed that such a scenario only leads to the production of Zn of up to [Zn/Fe] = 0, which remains inconsistent with observational results of [Zn/Fe] $\gtrsim 0.5$, as determined for EMP stars and HE 1327 -2326. Tominaga et al. (2007b) confirmed these results by introducing neutrino-transport into their MF SNe models of Pop III stars by artificially increasing Y_e in the complete Siburning region where Zn is produced. They showed that

increasing Y_e to >0.5 could indeed enhance the production of [Sc/Fe] > 0.3, as is observed in EMP stars, but could not simultaneously produce the enhanced [Zn/Fe] > 0 as well as [Co/Fe] > 0.

This suggests that the νp -process is not responsible for the enhanced Zn production in HE 1327–2326 and other EMP stars. Instead, the entire abundance pattern of HE 1327–2326 can be produced by rotation-driven, high-energy $(E=\times 10^{-51}\,\mathrm{erg})$ aspherical SNe with bipolar jets, as described in Sections 4.2 and 4.3. Nevertheless, the νp -process could contribute to an increased [Sr/Fe] ratio, as has been determined for HE 1327–2326 and other UMP stars.

5. Interpretation and Conclusions: Evidence for External Chemical Enrichment

Stellar abundance trends of various elements show increasing amounts of scatter with decreasing iron abundance. The fraction of stars with unusual abundance patterns is the highest at the lowest [Fe/H], with $\sim 80\%$ for [Fe/H] < -4.0, including HE 1327–2326. This has previously been interpreted as a result of inhomogeneous metal mixing or unusual SNe at the earliest times (Frebel & Norris 2015). On the contrary, the vast majority of metal-poor stars with [Fe/H] > -4.0 show patterns generally in line with a formation from well mixed gas (Cayrel et al. 2004; Yong et al. 2013). It is thus possible that these different types of abundance patterns are the result of different chemical enrichment channels that could have operated in the early universe. If one channel was common and the other rare, it might explain the extreme rarity of stars with [Fe/H] < -4.5, which still have a poorly understood origin scenario. This idea is principally supported by the fact that models for the metallicity ([Fe/H]) distribution function cannot reproduce the existence of the low-[Fe/H] tail with [Fe/ H] < -4.0 (Yong et al. 2013) simultaneously with the body of data on metal-poor stars with higher [Fe/H] abundances.

These challenges might be explained by the existence of aspherical Pop III SNe, as described in this work. The ejecta structure of a bipolar explosion is different than that of a quasispherical explosion, in that the high energy bipolar explosion produces high velocity ejecta along the polar axis as well as along the equatorial plane. These velocities can reach up to 4×10^4 km s⁻¹ and 8×10^3 km s⁻¹ after 50 s of the explosion, respectively (Tominaga 2009). This is higher than what can be maximally produced by faint mixing-fallback explosions $(4 \times 10^3 \,\mathrm{km \, s^{-1}})$ (Iwamoto et al. 2005). A high-velocity ejecta could facilitate carrying the SNe yields out of the parent host minihalo to enrich a neighboring minihalo. Theoretical studies have already explored this external enrichment channel across minihalos (Smith et al. 2015; Jeon et al. 2017; Hartwig et al. 2018). Assuming the gas in the neighboring system to be primordial, the abundance ratios of the supernova yields should largely remain preserved, such as the high [C/Fe] ratio in combination with the low iron abundances, as well as enhanced $[\alpha/Fe]$ and [Zn/Fe] values. Such a channel could have important implications for our understanding of the first chemical enrichment events and how these are preserved in second-generation UMP stars, especially those highly enhanced in carbon, such as the CEMP star HE 1327-2326.

An external enrichment scenario is principally supported by the outer halo nature of HE 1327–2326 and similar metal-poor stars. As such, they are likely accreted from some smaller now disrupted system, such as a primordial minihalo (Tissera et al.

2014; Battaglia et al. 2017; Frebel et al. 2019). The accretion origin of HE 1327–2326 is based on its proper motion values from the latest *Gaia* DR2 kinematic parameters for proper motions ($\mu_{\rm R.A.} = -52.52 \pm 0.04 \, {\rm mas \ yr}^{-1}$ and $\mu_{\rm decl.} = 45.50 \pm 0.04 \, {\rm mas \ yr}^{-1}$) and parallax ($\pi = 0.887 \pm 0.023 \, {\rm mas}$) used with a Galactic dynamical model (Carollo et al. 2014; Frebel et al. 2019).

Stars such as HE 1327–2326 might then have actually formed in these externally enriched neighboring primordial systems long before those were accreted into the Milky Way, as part of its own hierarchical growth. Future cosmological simulations will be able to provide additional insight into the nature of this channel, or provide alternative explanations for the formation sites of the second-generation CEMP stars with the lowest [Fe/H] abundances.

We thank the anonymous reviewer for the careful reading of our manuscript and the insightful comments and suggestions. We also thank Arthur Choplin, Volker Bromm, John Wise, Britton Smith, and Myoungwon Jeon for useful discussion. R. E., A.F., and I.U.R. acknowledge generous support for program *HST*-GO-14151 provided by a grant from STScI, which is operated by AURA, under NASA contract NAS 5-26555. R.E., A.F., I.U.R. and V.P. acknowledge support from JINA-CEE, funded in part by the National Science Foundation under Grant No. PHY-1430152. A.F. is supported by NSF-CAREER grant AST-1255160. I.U.R. acknowledges additional support from NSF grants AST-1613536 and AST-1815403.

Software: MOOG (Sneden 1973; Sobeck et al. 2011), MULTI (Carlsson 1986, 1992), MARCS (Gustafsson et al. 1975, 2008).

ORCID iDs

Rana Ezzeddine https://orcid.org/0000-0002-8504-8470
Anna Frebel https://orcid.org/0000-0002-2139-7145
Ian U. Roederer https://orcid.org/0000-0001-5107-8930
Nozomu Tominaga https://orcid.org/0000-0001-8537-3153
Jason Tumlinson https://orcid.org/0000-0002-7982-412X
Miho Ishigaki https://orcid.org/0000-0003-4656-0241
Ken'ichi Nomoto https://orcid.org/0000-0001-9553-0685
Vinicius M. Placco https://orcid.org/0000-0003-4479-1265
Wako Aoki https://orcid.org/0000-0002-8975-6829

References

Abohalima, A., & Frebel, A. 2018, ApJS, 238, 36
Aoki, W., Frebel, A., Christlieb, N., et al. 2006, ApJ, 639, 897
Asplund, M. 2005, ARA&A, 43, 481
Asplund, M., Grevesse, N., Sauval, A. J., & Scott, P. 2009, ARA&A, 47, 481
Barklem, P. S., Christlieb, N., Beers, T. C., et al. 2005, A&A, 439, 129
Battaglia, G., North, P., Jablonka, P., et al. 2017, A&A, 608, A145
Beers, T. C., & Christlieb, N. 2005, ARA&A, 43, 531
Bergemann, M., Lind, K., Collet, R., Magic, Z., & Asplund, M. 2012,
MNRAS, 427, 27

Bessell, M. S., Collet, R., Keller, S. C., et al. 2015, ApJL, 806, L16
Bromm, V., Yoshida, N., Hernquist, L., & McKee, C. F. 2009, Natur, 459, 49
Burrows, A., Ott, C. D., & Meakin, C. 2004, in Cosmic Explosions in three
Dimensions, ed. P. Höflich, P. Kumar, & J. C. Wheeler (Cambridge:
Cambridge Univ. Press), 209

Carlsson, M. 1986, A computer program for solving multi-level non-LTE radiative transfer problems in moving or static atmosphere, 33

Carlsson, M. 1992, in ASP Conf. Ser. 26, Cool Stars, Stellar Systems, and the Sun, ed. M. S. Giampapa & J. A. Bookbinder (San Francisco, CA: ASP) 499

Carollo, D., Freeman, K., Beers, T. C., et al. 2014, ApJ, 788, 180 Casey, A. R. 2014, PhD thesis, Australian National Univ.

```
Castelli, F., & Kurucz, R. L. 2004, astro-ph/0405087
Cayrel, R., Depagne, E., Spite, M., et al. 2004, A&A, 416, 1117
Choplin, A., Hirschi, R., Meynet, G., et al. 2018, A&A, 618, A133
Choplin, A., Hirschi, R., Meynet, G., & Ekström, S. 2017, A&A, 607, L3
Christlieb, N., Gustafsson, B., Korn, A. J., et al. 2004, ApJ, 603, 708
Cooke, R. J., & Madau, P. 2014, ApJ, 791, 116
Ekström, S., Meynet, G., Chiappini, C., Hirschi, R., & Maeder, A. 2008, A&A,
Ezzeddine, R., & Frebel, A. 2018, ApJ, 863, 168
Ezzeddine, R., Frebel, A., & Plez, B. 2017, ApJ, 847, 142
Fox, A. J. 2015, in COS Data Handbook, ed. S. Rose (Baltimore, MD: STScI)
Frebel, A., Aoki, W., Christlieb, N., et al. 2005, Natur, 434, 871
Frebel, A., Chiti, A., Ji, A. P., Jacobson, H. R., & Placco, V. M. 2015, ApJL,
Frebel, A., Collet, R., Eriksson, K., Christlieb, N., & Aoki, W. 2008, ApJ,
   684, 588
Frebel, A., Ji, A. P., Ezzeddine, R., et al. 2019, ApJ, 871, 146
Frebel, A., & Norris, J. E. 2015, ARA&A, 53, 631
Fröhlich, C., Hauser, P., Liebendörfer, M., et al. 2006b, ApJ, 637, 415
Fröhlich, C., Martínez-Pinedo, G., Liebendörfer, M., et al. 2006a, PhRvL, 96,
   142502
Fryer, C. L., & Heger, A. 2000, ApJ, 541, 1033
Gaia Collaboration, Brown, A. G. A., Vallenari, A., et al. 2018, A&A, 616, A1
Ghavamian, P., Aloisi, A., & Lennon, D. 2009, Preliminary Characterization of
  the Post- Launch Line Spread Function of COS, Tech. Rep.
Greif, T. H., Glover, S. C. O., Bromm, V., & Klessen, R. S. 2010, ApJ,
   716, 510
Grimmett, J. J., Heger, A., Karakas, A. I., & Müller, B. 2018, MNRAS,
Gustafsson, B., Bell, R. A., Eriksson, K., & Nordlund, A. 1975, A&A, 42, 407
Gustafsson, B., Edvardsson, B., Eriksson, K., et al. 2008, A&A, 486, 951
Hartwig, T., Bromm, V., Klessen, R. S., & Glover, S. C. O. 2015, MNRAS,
   447, 3892
Hartwig, T., Yoshida, N., Magg, M., et al. 2018, MNRAS, 478, 1795
Heger, A., & Woosley, S. E. 2010, ApJ, 724, 341
Hirai, Y., Saitoh, T. R., Ishimaru, Y., & Wanajo, S. 2018, ApJ, 855, 63
Hollek, J. K., Frebel, A., Roederer, I. U., et al. 2011, ApJ, 742, 54
Iwamoto, N., Umeda, H., Tominaga, N., Nomoto, K., & Maeda, K. 2005, Sci,
   309, 451
```

```
Jacobson, H. R., Keller, S., Frebel, A., et al. 2015, ApJ, 807, 171
Jeon, M., Besla, G., & Bromm, V. 2017, ApJ, 848, 85
Joggerst, C. C., Almgren, A., Bell, J., et al. 2010, ApJ, 709, 11
Keller, S. C., Bessell, M. S., Frebel, A., et al. 2014, Natur, 506, 463
Korn, A. J., Richard, O., Mashonkina, L., et al. 2009, ApJ, 698, 410
Maeda, K., & Nomoto, K. 2003, ApJ, 598, 1163
Maeder, A., Meynet, G., & Chiappini, C. 2015, A&A, 576, A56
Mashonkina, L., Gehren, T., Shi, J.-R., Korn, A. J., & Grupp, F. 2011, A&A,
  528, A87
Meynet, G., Ekström, S., & Maeder, A. 2006, A&A, 447, 623
Nomoto, K., Kobayashi, C., & Tominaga, N. 2013, ARA&A, 51, 457
Nordlander, T., Amarsi, A. M., Lind, K., et al. 2017, A&A, 597, A6
Omukai, K., & Palla, F. 2001, ApJL, 561, L55
Placco, V. M., Frebel, A., Beers, T. C., et al. 2016, ApJ, 833, 21
Pruet, J., Hoffman, R. D., Woosley, S. E., Janka, H.-T., & Buras, R. 2006, ApJ,
   644, 1028
Roederer, I. U., & Barklem, P. S. 2018, ApJ, 857, 2
Roederer, I. U., Placco, V. M., & Beers, T. C. 2016, ApJL, 824, L19
Smith, B. D., Wise, J. H., O'Shea, B. W., Norman, M. L., & Khochfar, S.
  2015, MNRAS, 452, 2822
Sneden, C. A. 1973, PhD thesis, Univ. Texas at Austin
Snyder, E., & Sonnentrucker, P. 2017, Analysis of the COS/NUV Extraction
  Box Heights (Baltimore, MD: STScI)
Sobeck, J. S., Kraft, R. P., Sneden, C., et al. 2011, AJ, 141, 175
Stacy, A., Bromm, V., & Loeb, A. 2011, MNRAS, 413, 543
Stacy, A., Greif, T. H., & Bromm, V. 2012, MNRAS, 422, 290
Takeda, Y., Hashimoto, O., Taguchi, H., et al. 2005, PASJ, 57, 751
Thévenin, F., & Idiart, T. P. 1999, ApJ, 521, 753
Tissera, P. B., Beers, T. C., Carollo, D., & Scannapieco, C. 2014, MNRAS,
  439, 3128
Tominaga, N. 2009, ApJ, 690, 526
Tominaga, N., Maeda, K., Umeda, H., et al. 2007a, ApJL, 657, L77
Tominaga, N., Umeda, H., & Nomoto, K. 2007b, ApJ, 660, 516
Tsujimoto, T., & Nishimura, N. 2018, ApJL, 863, L27
Umeda, H., & Nomoto, K. 2002, ApJ, 565, 385
Woosley, S. E., & Weaver, T. A. 1995, ApJS, 101, 181
Yong, D., Norris, J. E., Bessell, M. S., et al. 2013, ApJ, 762, 27
Yoshida, N., Omukai, K., Hernquist, L., & Abel, T. 2006, ApJ, 652, 6
```